ADVANCED HEALTHCARE MATERIALS
www.advhealthmat.de

Skin-Interfaced Microfluidic Systems that Combine Hard and Soft Materials for Demanding Applications in Sweat Capture and Analysis

*Jungil Choi, Shulin Chen, Yujun Deng, Yeguang Xue, Jonathan T. Reeder, Daniel Franklin, Yong Suk Oh, Jeffrey B. Model, Alexander J. Aranyosi, Stephen P. Lee, Roozbeh Ghaffari, Yonggang Huang, and John A. Rogers**

Eccrine sweat contains a rich blend of electrolytes, metabolites, proteins, metal ions, and other biomarkers. Changes in the concentrations of these chemical species can indicate alterations in hydration status and they can also reflect health conditions such as cystic fibrosis, schizophrenia, and depression. Recent advances in soft, skin-interfaced microfluidic systems enable real-time measurement of local sweat loss and sweat biomarker concentrations, with a wide range of applications in healthcare. Uses in certain contexts involve, however, physical impacts on the body that can dynamically deform these platforms, with adverse effects on measurement reliability. The work presented here overcomes this limitation through the use of microfluidic structures constructed in relatively high modulus polymers, and designed in geometries that offer soft, system level mechanics when embedded low modulus elastomers. Analytical models and finite element analysis quantitatively define the relevant mechanics of these systems, and serve as the basis for layouts optimized to allow robust operation in demanding, rugged scenarios such as those encountered in football, while preserving mechanical stretchability for comfortable, water-tight bonding to the skin. Benchtop testing and on-body field studies of measurements of sweat loss and chloride concentration under imposed mechanical stresses and impacts demonstrate the key features of these platforms.

1. Introduction

Electronic, optoelectronic, colorimetric, and/or microfluidic biosensors that interface with the skin offer unique capabilities in measuring physiological, kinematic, and environmental signals across applications in healthcare, sports, consumer wellness, and military training.[1] Such devices support versatile options in ambulatory monitoring and in managing a variety of conditions, continuously and in real-time outside of hospital

Prof. J. Choi
School of Mechanical Engineering
Kookmin University
Seoul 02707, Republic of Korea

S. Chen, Prof. R. Ghaffari, Prof. J. A. Rogers
Department of Biomedical Engineering
Northwestern University
Evanston, IL 60208, USA
E-mail: jrogers@northwestern.edu

S. Chen, Dr. J. T. Reeder, Dr. D. Franklin, Dr. Y. S. Oh, J. B. Model, Dr. A. J. Aranyosi, S. P. Lee, Prof. R. Ghaffari, Prof. J. A. Rogers
Querrey-Simpson Institute for Bioelectronics
Northwestern University
Evanston, IL 60208, USA

Dr. Y. Deng
State Key Laboratory of Mechanical System and Vibration
Shanghai Jiao Tong University
Shanghai 200240, China

The ORCID identification number(s) for the author(s) of this article can be found under https://doi.org/10.1002/adhm.202000722

DOI: 10.1002/adhm.202000722

Dr. Y. Deng, Dr. Y. Xue, Prof. Y. Huang
Department of Civil and Environmental Engineering
Mechanical Engineering
and Materials Science and Engineering
Northwestern University
Evanston, IL 60208, USA

Dr. J. T. Reeder, Dr. D. Franklin, Dr. Y. S. Oh, Prof. J. A. Rogers
Department of Materials Science and Engineering
Northwestern University
Evanston, IL 60208, USA

J. B. Model, Dr. A. J. Aranyosi, S. P. Lee, Prof. R. Ghaffari
Epicore Biosystems, Inc.
Cambridge, MA 02139, USA

Prof. J. A. Rogers
Departments of Chemistry
Biomedical Engineering and Electrical Engineering and Computer Science
Northwestern University
Evanston, IL 60208, USA

Prof. J. A. Rogers
Department of Neurological Surgery
Northwestern University
Evanston, IL 60208, USA

settings. Advanced platforms include options for hydration/biochemical analysis of blood, interstitial fluid, and/or sweat biochemistry.[2] Among these biofluids, sweat is of interest for its ability for noninvasive collection and for its rich, although in some cases not fully understood, biochemical information content. Conventional technologies for sweat collection rely on adhesive tapes, wicking gauzes, absorbent pads, and centrifuge systems, with separate laboratory instruments for analysis. These approaches support some basic level of measurement capabilities relevant for studies in controlled laboratory settings, but they are not suitable for precise evaluations or for remote or ambulatory deployments.

Recent progress in skin-interfaced electrochemical and microfluidic sensors overcome these limitations, to allow for continuous and/or intermittent assessment of sweat dynamics and sweat chemistry with the ability to track health and performance in real-world environments.[3] A particularly powerful class of platform exploits concepts in soft microfluidics, where low modulus elastomers define networks of microchannels, microreservoirs, valves, analysis chemistries, and other features adapted from traditional, rigid lab-on-a-chip diagnostic technologies. The results allow for capture, collection, and evaluation of pristine microliter volumes of sweat directly from the surface of the skin via an intimate mechanical coupling and watertight seal to the epidermis.[4] Although these platforms support unique modes of operation relative to alternatives, their inherently soft and elastic physical properties can lead to deformations and distortions upon direct mechanical impacts and/or extreme stresses during intense scenarios sometimes encountered in military training, contact sports, and related activities.[5] Such effects can cause uncontrolled flow and movement of sweat within the microfluidic structures, often in ways that can adversely affect the measurement accuracy, precision, and reliability.

This paper introduces a set of materials and mechanics design concepts that addresses these challenges, without compromising the critically important soft adhesive interface to the skin. Here, micromachined and lithographically patterned structures in polyurathene (PU) resin define microfluidic components with sufficient stiffness to maintain fixed cross-sectional dimensions associated with internal structures, even under significant mechanical loads. In compuationally optimized serpentine layouts, these structures support soft, stretchable mechanics at the system level when embedded in thin elastomeric matrices. In these designs, the microfluidic structure represents a rigid, but deformable, "skeletal" structure surrounded by a low modulus polymer that provides an elastic restoring force and a conformal interface to the skin. These features serve as the foundation for a mechanically robust, skin-compatible system that is highly insensitive to physical impacts or other forces encountered even in extreme use scenarios. Quantitative analysis of the mechanics of these hard/soft materials systems defines the underlying considerations and guides optimized selection of design choices. Benchtop studies and field trials in physically demanding conditions illustrate the operational properties.

2. Results and Discussion

2.1. Layout and Fabrication

The platforms involve microfluidic constructs formed in a photocurable PU resin (Norland Optical Adhesive, NOA) and embedded in a thin, soft, elastomeric encapsulating structure (**Figure 1**a,b). The fabrication begins with formation of a mold in poly(dimethylsiloxane) (PDMS) in the overall geometry of the microfluidic system. Spin-casting and photocuring a layer of PU with thickness of 450 μm on this mold (Figure S1, Supporting Information) and then removing the cured material yields a structure that can be capped with a thin (200 μm) layer of the same PU to define a closed microchannel structure, according to procedures outlined in the Experimental Section. The fully cured PU presents a hydrophilic surface, with a water contact angle of 73° ± 0.1° (Figure S2, Supporting Information). For the examples presented here, the structure consists of serpentine shaped channels with inner widths and heights of 520 and 250 μm, respectively (Figure 1c). From this platform, a pulsed laser system cuts the PU in a geometry that matches that of the microchannels, but with a spacing of 300 μm to thereby define the lateral thickness of the walls of the microchannels. As such, the total thickness and width of the structures are 650 μm and 1.12 mm, respectively (Figure S3a, Supporting Information). The serpentine geometry provides mechanical stretchability, following principles well established in the field of stretchable electronics.[6]

This structure mounts on a uniform base layer of PDMS (400 μm thick, with white pigment; 1 MPa) with two circular inlet ports (1 mm diameter) that align with similar openings formed in a bottom adhesive (60 μm thick, 3D 1524, ≈17 kPa) that bonds to the PDMS on one side and to the skin on the other. These inlets connect to openings in microchannels of two separate serpentine structures, one for measurement of sweat volume and the other for assessment of sweat chloride concentration. The PDMS/adhesive forms a low modulus interface for intimate coupling between the microfluidic channel inlet ports and the skin (Figure 1d). A soft formulation of a transparent silicone elastomer (Ecoflex; 60 kPa) with thickness of 400 μm serves as a top encapsulation layer. A colored dye and a chloride assay, both separately preinjected near the inlet regions of each microchannel structure, allow for colorimetric analysis of local sweat loss and chloride concentration, respectively. A color reference marker on a top graphics layer enables color matching and analysis of chloride concentrations under different lighting conditions.

2.2. Mechanics Considerations

The design goal is to reduce the volume change of the microchannel structures under various types of mechanical deformations, while achieving overall flexibility and stretchability. The deformations caused by normal pressures on the device surface can be reduced by using a PU material (NOA) with a relatively high modulus (1.1 GPa) as the structural component of the microchannel. The volume change of the microchannel (ΔV) under a normal

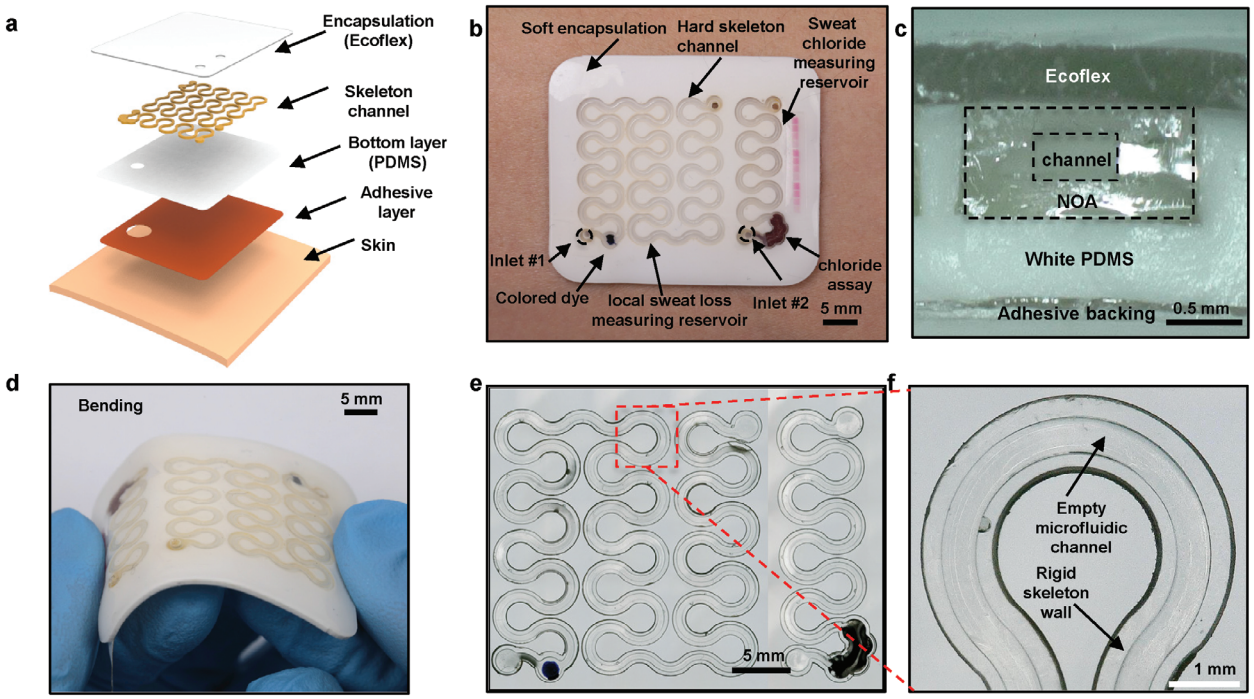

Figure 1. a) Schematic illustration of a soft microfluidic device that incorporates a hard microchannel structure defined in a serpentine shape (Peano fractal geometry) and embedded in an elastomer, bonded to the skin with an adhesive layer. Two inlet ports lead to two separate microchannels. b) Optical image of such a "skeletal" device designed to measure local sweat loss and sweat chloride concentration. c) Schematic drawing of the device showing the dimensions of the rigid PU microchannel structure, top silicone encapsulation layer (Ecoflex), and a white PDMS substrate. d) Optical image of a device under mechanical deformation. e) Optical image of a device highlighting the microfluidic channels created by laser cutting. f) Magnified image of a microfluidic channel showing the channel and rigid PU bonded at the boundary.

pressure P_{out} can be obtained from a beam model that neglects the extremely soft Ecoflex encapsulation as

$$\frac{\epsilon V}{V_0} = \frac{1}{60}\frac{P_{out}}{\bar{E}_{NOA}}\left(\frac{w_{ch}}{t_{NOA}}\right)^3\frac{w_{ch}}{h_{ch}} \quad (1)$$

where V_0 is the initial volume of the microchannel, w_{ch} and h_{ch} are the width and height of the microchannel, and t_{NOA} (as shown in **Figure 2**a) and $\bar{E}_{NOA} = \frac{E_{NOA}}{1-\nu_{NOA}^2}$ are the top thickness and plane-strain modulus of the microchannel, respectively (E_{NOA} – Young's modulus, and ν_{NOA} – Poisson's ratio). The volume change is inversely proportional to the bending stiffness $\bar{E}_{NOA}t_{NOA}^3$ of the microchannel cover (NOA layer) such that the volume change is negligible for a sufficiently thick cover. The following parameters are fixed in the device design: $t_{NOA} = 200$ µm, $w_{ch} = 528$ µm, and $h_{ch} = 250$ µm, which gives the volume change to be less than 0.01% for the pressure up to 100 kPa (a relatively high pressure on the skin that can trigger human attention during normal workout conditions).

The key geometric parameters of the serpentine structures include the outer width w_{sk} and inner width w_{ch} of the microchannel, the radius R and arc angle α of the serpentine, and the spacing D between parallel serpentines, as shown in Figure 2a. In response to stretching, the deformation of the serpentine structure is dominated by in-plane bending. Decreasing $\frac{w_{ch}}{w_{sk}}$ or increasing $\frac{R}{w_{sk}}$ will enhance the bending stiffness of the serpentine structure, therefore reduce the deformation hence the volume change of the microchannels. As shown in Figure 2b,c, for $\frac{w_{ch}}{w_{sk}} \leq 0.5$ and $\frac{R}{w_{sk}} \geq 1.5$ ($\alpha = 0°$), the volume change is less than ≈0.1% under 20% uniaxial stretching (approximately maximum stretching on the skin). This result indicates that the serpentine shaped microchannels are effective in reducing the volume change under in-plane stretching.

The serpentine structure should also not self-contact, which sets the following geometric constraints

$$\begin{aligned} &2R + w_{sk} \leq 4R\cos\alpha, \\ &D \geq \left(2R + 2R\sin\alpha + w_{sk}\right) \end{aligned} \quad (2)$$

A compact design should additionally achieve a large percentage of coverage area of the serpentine structure, defined by the ratio χ of the coverage area of serpentine structure to the entire device above a critical value χ_{cr}

$$\chi = \frac{(\pi + 2\alpha)\, w_{sk}}{2D\cos\alpha} \geq \chi_{cr} \quad (3)$$

For $\chi_{cr} = 0.5$, the in-equalities above, together with $D = (2R + 2R\sin\alpha + w_{sk})$, give the design diagram in Figure 2d for $\frac{R}{w_{sk}}$ and α. The blue region represents the acceptable design and the red star indicates the optimum design with maximum $\frac{R}{w_{sk}}$ and α. The blue star indicates the device reported here, and it is close to the optimum design.

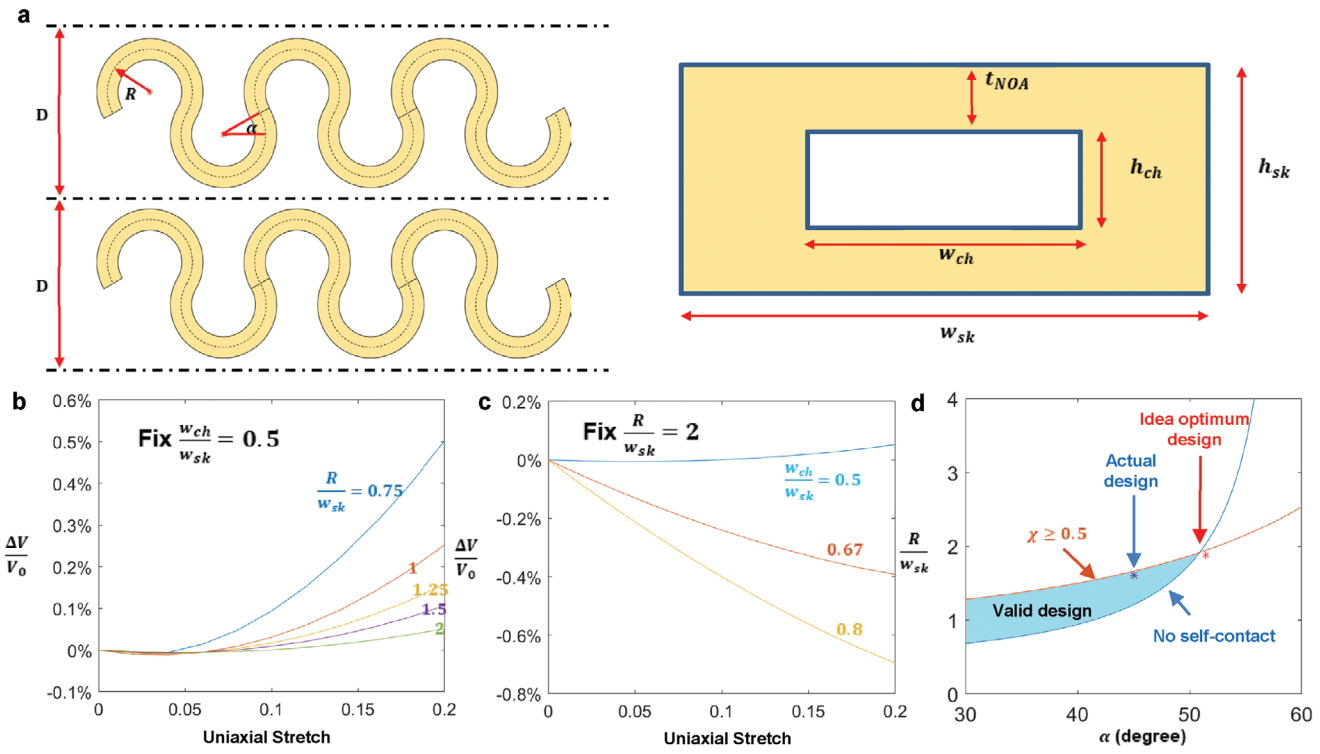

Figure 2. a) Top view and cross-sectional diagram for mechanics modeling of serpentine microchannel structures. b) Effect of $\frac{R}{w_{sk}}$ on the change in channel volume under uniaxial stretching. c) Effect of $\frac{w_{ch}}{w_{sk}}$ on the change in channel volume under uniaxial stretching. d) Design diagram for α and $\frac{R}{w_{sk}}$ under geometrical constraints. The light blue region shows the acceptable zone of design. The red star marks the optimum design and the blue star marks the actual design of the devices reported here.

2.3. Mechanical Characteristics

The overall serpentine layout corresponds to a Peano fractal of second order with a configuration that enhances biaxial stretchability.[7] A benchtop apparatus that applies variable biaxial strains allows for quantitative studies of the mechanical characteristics of these systems. For evaluation the effects of the skeletal structure, PDMS serves as the material for a comparison device that involves a similar layout, with total thickness of 650 μm (Figure S3b, Supporting Information). The effective Young's moduli of the system are 1.4 ± 0.06 and 1.3 ± 0.02 MPa for tensile deformation along the *x*-axis and *y*-axis directions, respectively (**Figure 3**a,c). As skin-interfaced microfluidic systems typically collect sweat from body locations with relatively flat surfaces such as the forearm, back, thigh, chest, a maximum strain of 10% in this test spans physiologically relevant values. The device with PU microchannels in otherwise identical geometric designs, referred as the skeletal device, has effective moduli of 1.1 ± 0.16 and 1.4 ± 0.20 MPa along the *x*-axis and *y*-axis, respectively. The modulus along the *x*-axis direction is smaller than that of PDMS device because the material for the top encapsulation has a modulus lower than that of the PDMS. The serpentine shape of the PU microchannels minimizes their influence on the mechanics. The effective modulus of the skeletal device along the *y*-axis direction is slightly larger than that along the *x*-axis. Here, the PU structures along the *x*-axis are not connected. The low modulus of the material in between leads to localization of deformations to this region upon stretching. Overall, the skeletal device has a modulus similar to the PDMS device. For the same loading conditions as in experiments, finite element analysis (FEA) predicts an equivalent modulus 1.1 MPa along *x*-axis and 1.5 MPa along *y*-axis (Figure S5a, Supporting Information), which agree reasonably well with experimental measurements without any parameter fitting.

Three-point bending stiffness tests yield the modulus of elasticity under bending conditions. The PDMS device has a slope of force displacement of 0.018 ± 0.003 and 0.014 ± 0.004 N mm^{-1} in the *x*-axis direction and *y*-axis direction directions, respectively (Figure 3b,c). The corresponding values for the skeletal device are 0.03 ± 0.005 and 0.05 ± 0.02 N m^{-1}, respectively. The skeletal device is only 2–4 times stiffer than the PDMS device, despite a modulus of the PU that is ≈1000 times greater than that of the PDMS, because of the serpentine geometry. For the three-point bending test, FEA predicts an initial slope of the force–displacement of 0.038 N mm^{-1} for bending along the *x*-axis direction and 0.052 N mm^{-1} for bending along *y*-axis direction (Figure S5b, Supporting Information), in a reasonable agreement with experiment.

The strain distributions obtained by FEA, shown in Figure 3d–g, highlight various mechanical deformations of a skeletal structure (Figure 3d,e; Figure S6, Supporting Information) and an encapsulated skeletal device (Figure 3f,g). For stretching up to 15% and for three-point bending with a maximum displacement of 5 mm, maximum principle strains in the PU are only 2.3% and

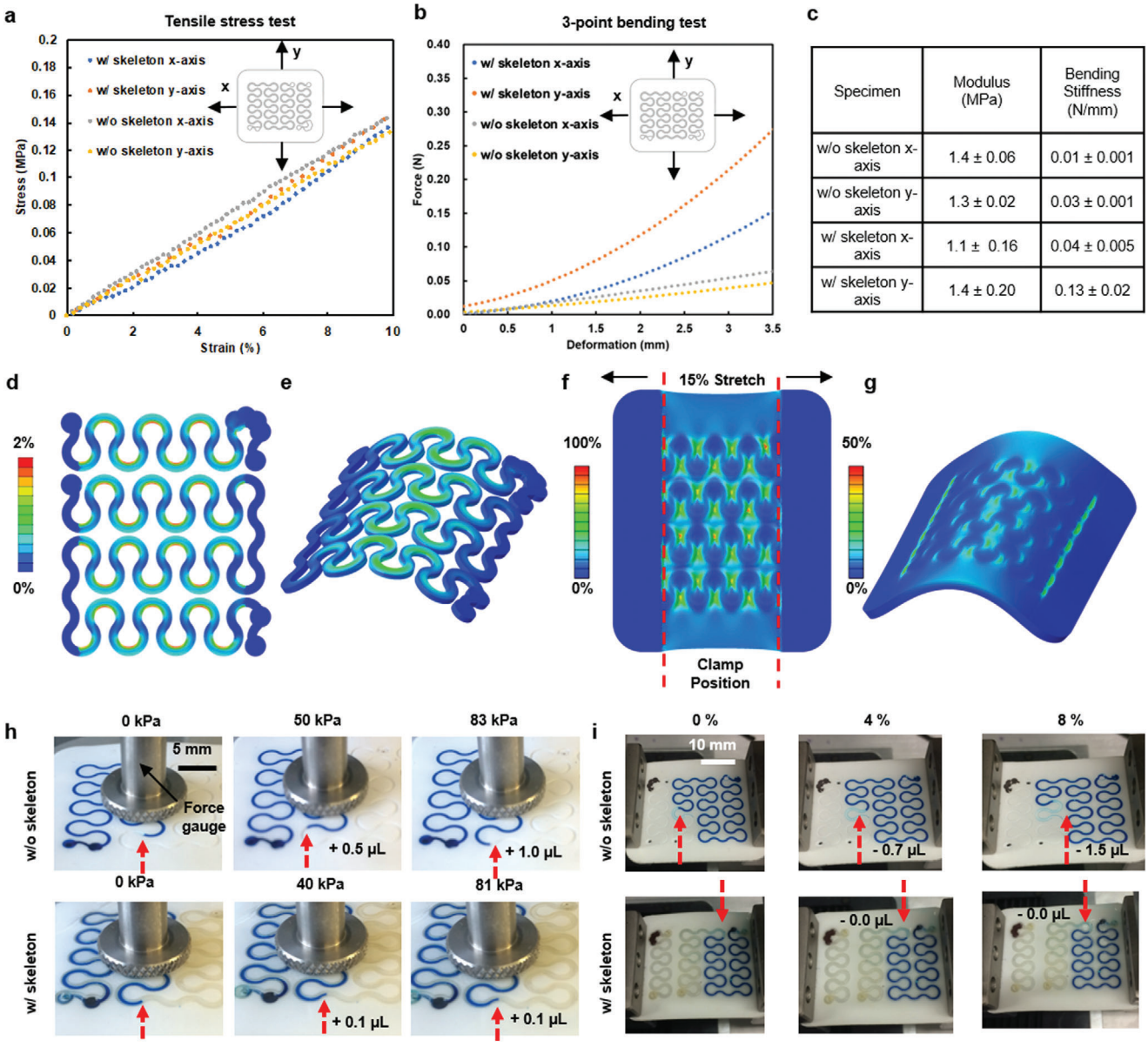

Specimen	Modulus (MPa)	Bending Stiffness (N/mm)
w/o skeleton x-axis	1.4 ± 0.06	0.01 ± 0.001
w/o skeleton y-axis	1.3 ± 0.02	0.03 ± 0.001
w/ skeleton x-axis	1.1 ± 0.16	0.04 ± 0.005
w/ skeleton y-axis	1.4 ± 0.20	0.13 ± 0.02

Figure 3. Experimental results for a) tensile stress/strain tests and b) three-point bending tests of a PDMS device and a skeletal device in two directions, and c) modulus and bending stiffness. FEA results for the strain distribution in the skeletal structures at d) 15% stretching along *y*-axis direction and e) three-point bending with a maximum displacement of 5 mm; and strain distributions in the entire structures including the encapsulations at f) 15% stretching along *y*-axis direction and g) three-point bending with a maximum displacement of 5 mm. h) Optical images of pressing a PDMS device and a skeletal device filled with colored dyes in water using the tip of a force gauge. i) Optical images of a PDMS device and a skeletal device filled with colored dyes in water during stretching along the *x*-axis.

1.2%, respectively, which are small such that the volume changes of microchannels are also small.

2.4. Performance under Mechanical Loads

Applied normal pressures such as those encountered in certain applications can induce deformations in the microchannels and cause associated uncontrolled displacements of fluids located within them, thereby producing measurement uncertainties. Benchtop measurements compare the behaviors of skeletal to PDMS devices with otherwise identical designs. Studies examine the effects of pressures from 0 to 80 kPa over areas of ≈111 mm^2 in circular shapes along a partially filled serpentine channel. The PDMS device exhibits a change in volume of the contacted area of ≈1.0 ± 0.1 µL (Figure 3h), as estimated from the forward motion of the filling front due to the applied pressure. By contrast, the skeletal design shows a change in volume that is less than ≈0.1 µL, below the limit of detection. Similar

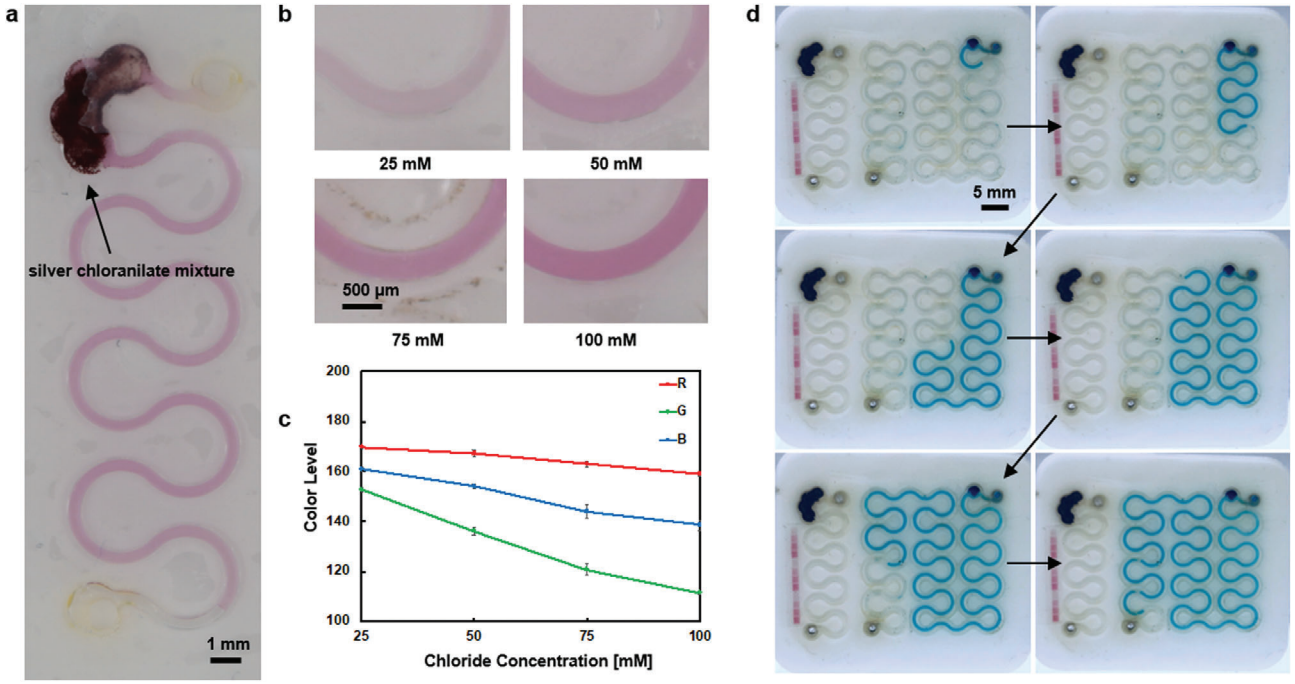

Figure 4. Optical images of color development of a) assay microreservoirs as a function of b) chloride concentration and c) color level for each case. d) Optical images of filling of colored dyes in water into the sweat loss measurement reservoir.

improvements were observed for stretching deformations, where the PDMS device shows changes in volume of -1.5 ± 0.1 µL at 8% of strain, causing the position of the filling front to shift in position by ≈10 mm (Figure 3i). By contrast, the skeletal design shows no measurable change for similar levels of stretching at 8% of strain. FEA simulation confirms negligible changes in volume for the skeletal structures under stretching or bending along both the *x* and *y* directions (Figure S7, Supporting Information).

2.5. Colorimetric Analysis of Electrolyte Concentrations and Local Sweat Loss

Colorimetric assays provide simple means for real-time analysis of sweat biomarkers, without requirements for electronics or power supply.[5a] In the example illustrated here, silver chloranilate serves as an assay for quantifying chloride concentration (**Figure 4**a). Reaction with chloride ions in sweat yield chloranilate ions, to create a purple color that has an optical density proportional to the concentration of chloride (Figure 4b). Silver chloranilate mixed with pHEMA gel immobilizes the assay chemistry at the inlet of the microchannel for chloride analysis. As sweat enters the device, it mixes with this suspension, causing a change in color as a byproduct of the reaction. The color density from the assay is proportional to the chloride concentration in sweat. Color reference markers printed as a graphics layer on the top surface of the device facilitate quantification of this color response from digital images, even under variable lighting conditions (Figure 4c).[5a] Dehydrated dye deposited at the inlet of the microchannel for measuring sweat loss mixes with sweat as it flows into the device, thereby allowing visual tracking of the filling front (Figure 4d). As an alternative option, the top surfaces of the microchannels can be constructed with microstructural relief features that provide retroreflection microstructures within the channels to enable optical detection of sweat flow without the dye (Figure S8, Supporting Information). The advantage of this approach is that it enables multiple cycles of use of the device.

2.6. Field Studies of Soft Skeletal Microfluidic Devices

Field studies on healthy volunteers during cycling exercises and subsequent mechanical events demonstrate aspects of operation and performance in real-world applications. As with mechanical evaluations, these tests include comparative analysis using an otherwise similar device constructed in PDMS, with both platforms attached to the anterior region of the forearm during a 30 min high intensity exercise session. Sweat from the skin fills the microfluidic channels of the PDMS and skeletal devices in a similar manner during this time period. Manually applied mechanical forces yield results that define the robustness of operation (Figure 5a). Pressing with a fingertip leads to displacements of sweat by volume of $\approx 2.4 \pm 0.1$ µL from 10.9 µL and $\approx 0.1 \pm 0.1$ µL from 8.0 µL for the PDMS and skeletal device, respectively. Direct impacts delivered to a PDMS device with a fist disrupt the embedded bioassay suspensions, resulting in the propagation of chemical reagents (e.g., silver chloranilate) through the microchannel in an uncontrolled manner. Similar impacts to the skeletal device have no effect.

In addition to different responses to external forces, these two device platforms exhibit dramatically different rates of evaporation of sweat. Demonstrations to highlight these differences

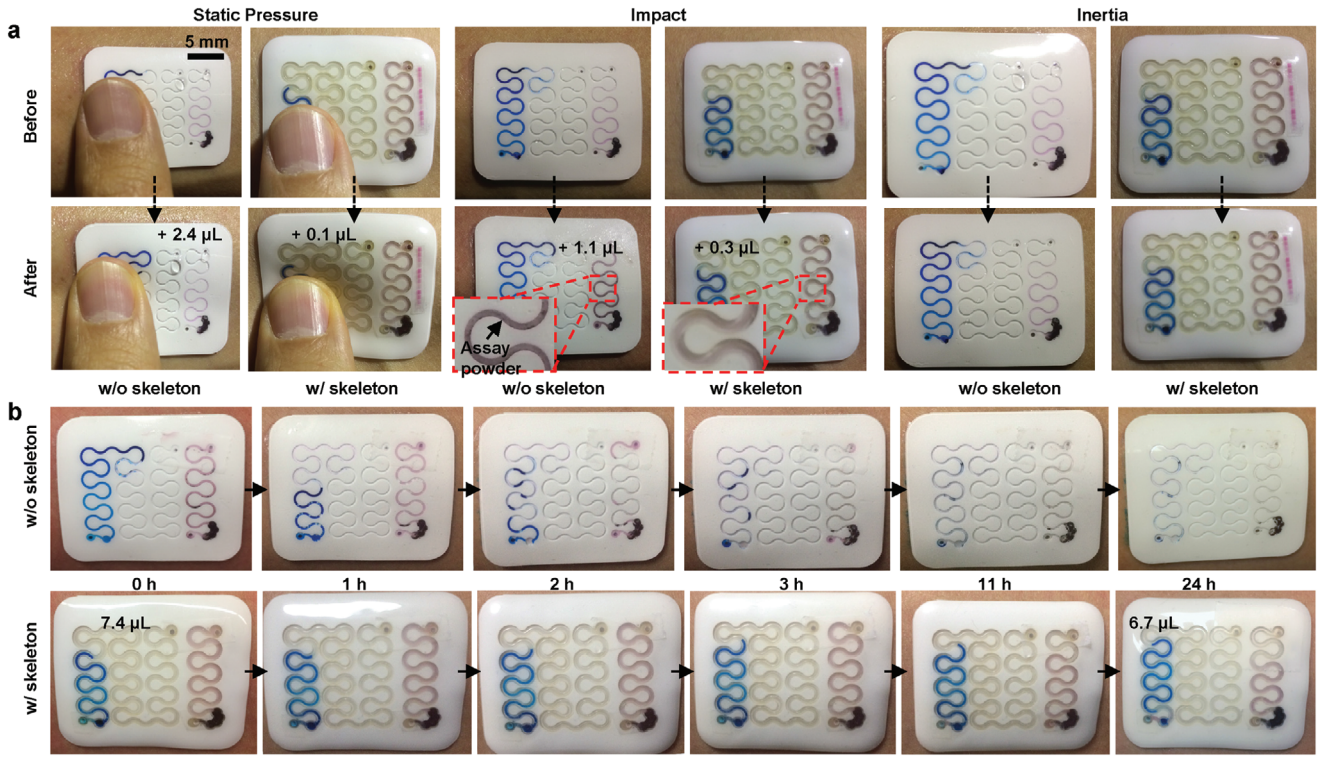

Figure 5. Optical images of a PDMS device and a skeletal device after sampling sweat in trials under various mechanical stresses: a) static compression test using a thumb, impact test, inertia test, and b) evaporation test after trials.

involve leaving the PDMS and skeletal devices on the skin under ambient conditions (20 °C, relative humidity 40%) with sweat contained within the microchannels (Figure 5b). Application of acrylic thin film adhesives (3M magic tape) seals the outlets to prevent evaporation through these openings. Sweat in the PDMS device evaporates quickly, leaving ≈45% of the volume after 1 h and only <5% after 3 h, with complete evaporation after 11 h. By contrast, sweat stored in the microchannels of the skeletal device decreases by only 10% after 24 h. This result demonstrates that the PU microchannels are ≈100 times less permeable than those constructed in PDMS.[8]

3. Conclusions

This study introduces a hard/soft composite structure as the basis for a soft, skin-interfaced microfluidic device that allows for robust capture and colorimetric analysis of sweat chloride and local sweat loss even under mechanical stresses and impacts. Here, microfluidic channels formed in high modulus, impermeable polymers and in serpentine geometries reside in a thin matrix of a soft elastomer to yield a rugged, yet comfortable and water-tight interface to the skin. Detailed experimental and computational studies of the mechanics of these systems define all of the key considerations and also provide comparison against conventional soft microfluidic devices for previously reported for these applications. Field trials on healthy and active subjects demonstrate the key capabilities in realistic modes of use and under simulated mechanical stresses and impacts that could occur during intensive physical exercise and contact sports. These results, and their straightforward application to related but more sophisticated types of skin-interfaced microfluidic platforms, have the potential to address requirements across many high intensity activities such as military training, combat, and various contact sports.

4. Experimental Section

Fabrication Process: The fabrication began with fabrication of a silicon mold by spin-coating a layer of photoresist (KMPR 1010, Microchem, MA, USA) at 3000 rpm for 30 s on a silicon wafer (1.5 mm thickness), performing photolithography and then deep reactive ion etching (STS Pegasus ICP-DRIE; SPTS Technologies, Newport, UK) to define features of relief in the silicon to a depth of 250 µm. Spin-coating poly(methylmethacrylate) (PMMA; Microchem, MA, USA) at 3000 rpm followed by curing at 180 °C generated a layer to facilitate demolding of PDMS (Sylgard 184; Dow corning, MI, USA; mixing ratio of base to curing agent: 10:1) spin-cast at 200 rpm and thermally cured at 150 °C for 3 min. Removing the PDMS completed the fabrication of a corresponding mold for the photocurable PU. A laboratory corona treatment system (Electro-Technic Products, IL, USA) activated the surface of PDMS, such that application of a vacuum in a chamber with trichloro(1H,1H,2H,2H-perfluorooctyl)silane (Sigma-Aldrich, MO, USA) for 4 h, generated a self-assembled monolayer of silane. Pouring UV-curable resin (NOA 61, Norland Products, NJ, USA) on the PDMS with a spacer (200 µm film) followed by exposure to UV light with 365 nm wavelength (NailStar Professional, USA) at a power of 36 W for 2 min partially cured the NOA film. Performing the same process on a bare layer of PDMS generated a partially cured uniform layer of NOA. Laminating these two layers of NOA together and exposing them to UV light for 12 h generated a closed microfluidic channel structure in NOA.

An automated cutting system based on a pulsed laser (LPKF ProtoLaser R, Germany) defined the outline of the serpentine skeletal geometry from the NOA microchannel system. Pouring PDMS (Sylgard 184; Dow corning, MI, USA; mixing ratio of base to curing agent: 10:1) mixed with white silicone dye (Reynolds Advanced Materials) at 10% wt on the PMMA-coated silicon wafer and spin-casting at 300 rpm generated a bottom substrate layer with thickness of 250 µm. Corona treating the NOA skeletal and the white PDMS layer enabled strong bonding between them. Pouring a low modulus silicone precursor (Ecoflex 35) on top after corona treatment, spinning at 150 rpm and thermally curing formed a top encapsulation layer with thickness of 300 µm. A CO_2 laser cutter (Universal Laser Systems, AZ, USA) defined the outer perimeter of the device platform and created the inlet and the outlet regions. A skin adhesive (1524; 3M, MN, USA; thickness 60 µm) bonded to the bottom surface of the device using a corona treatment process. The same process for fabrication the silicon mold, but performed with an inverted photomask yields a mold for the PDMS microfluidic device as the control.

Colorimetric Assay Formulation: Food dye (2 µL) applied to the inlet region of the microchannel structure for measuring sweat loss provided coloration to facilitate visual tracking of the filling process. An 8 µL volume of a mixture of 100 mg of silver chloranilate (MP Biomedicals, CA, USA) and 400 µL of 2% polyhydroxyethylmethacrylate (pHEMA, Mv 300000: Sigma-Aldrich, MO, USA) placed near the inlet region of the microchannel for chloride detection served as a colorimetric assay.

Mechanical Testing of the Exoskeletal-Structured Device: A tensile tester (20G: MTS Sintech) allowed tensile stress/strain tests and three-point bending stiffness tests. A custom stage enabled the stretching tests. A force gauge (Mark-10, NY, USA) served as the basis for pressing tests.

Finite Element Analysis: 3D FEA was used to study the performance of the skeletal device. The materials used in FEA include NOA (Young's modulus 1.1 GPa, Poisson's ratio 0.34), Ecoflex (Young's modulus 60 kPa, Poisson's ratio 0.49), and PDMS (Young's modulus 1 MPa, Poisson's ratio 0.49). Pseudoelements with extremely low modulus (<1/1000 of Ecoflex modulus) filled the microfluidic channels to calculate the internal volume change without interfering the deformation in these regions.

Analytical Model of Serpentine Shaped Patterns under In-Plane Stretching: Considering the skeletal structure in a unit cell, the force equilibrium of the curved beam gives the normal traction force N and momentum M in the beam as

$$\begin{aligned} N(\theta) &= P\cos\theta, \\ M(\theta) &= PR(\cos\theta + \sin\alpha) \end{aligned} \tag{4}$$

where P is the applied force, R and α are the radius and the arc angle of the serpentine structure, respectively, and θ is the angle in the polar coordinate (Figure S9, Supporting Information). The elastic energy is then given by

$$U = \int_0^{\frac{\pi}{2}+\alpha} \left[\frac{N^2}{2\bar{E}_{\mathrm{NOA}}A^*} + \frac{M^2}{2\bar{E}_{\mathrm{NOA}}I^*} \right] R\mathrm{d}\theta \tag{5}$$

Here for the skeletal structure, considering the extruded channel space, its cross-sectional area A^* and bending moment of inertia I^* are given by

$$A^* = w_{\mathrm{sk}}\, h_{\mathrm{sk}} - w_{\mathrm{ch}}\, h_{\mathrm{ch}} = w_{\mathrm{sk}}\, h_{\mathrm{sk}}\,(1-\xi\eta) \tag{6}$$

$$I^* = \frac{w_{\mathrm{sk}}^3 h_{\mathrm{sk}}}{12} - \frac{w_{\mathrm{ch}}^3 h_{\mathrm{ch}}}{12} = \frac{w_{\mathrm{sk}}^3 h_{\mathrm{sk}}}{12}\left(1-\xi^3\eta\right) \tag{7}$$

where $\xi = \frac{w_{\mathrm{ch}}}{w_{\mathrm{sk}}}$ and $\eta = \frac{h_{\mathrm{ch}}}{h_{\mathrm{sk}}}$. The displacement u_0 due to P can be obtained from the energy method as

$$u_0 = \frac{\partial U}{\partial P} = \frac{PR^3}{4\bar{E}_{\mathrm{NOA}}} \left[\frac{\pi + 2\alpha - \sin 2\alpha}{A^* R^2} + \frac{(\pi+2\alpha)(2-\cos 2\alpha) + 3\sin 2\alpha}{I^*} \right] \tag{8}$$

The displacement u_0 in the unit cell can also be related to the applied uniaxial strain $\varepsilon_{\mathrm{app}}$ by

$$\varepsilon_{\mathrm{app}} = \frac{u_0}{R\cos\alpha} \tag{9}$$

For skeletal channel layer, the effective modulus is then calculated with

$$E_{\mathrm{eff}} = \frac{\frac{P}{Dh_{\mathrm{sk}}}}{\varepsilon_{\mathrm{app}}} \tag{10}$$

where D is the spacing between parallel serpentines and h_{sk} is the height of the skeletal structure (Figure 2a). The normalized effective modulus is then given by

$$\frac{E_{\mathrm{eff}}}{E} = \frac{\cos\alpha\left(\frac{w_{\mathrm{sk}}}{R}\right)^3}{3\left(\frac{D}{R}\right)\left[\frac{\pi+2\alpha-\sin 2\alpha}{12(1-\xi\eta)}\left(\frac{w_{\mathrm{sk}}}{R}\right)^2 + \frac{(\pi+2\alpha)(2-\cos 2\alpha)+3\sin 2\alpha}{\left(1-\xi^3\eta\right)}\right]} \tag{11}$$

For fixed $\xi = 0.5$, $\eta = 0.5$, and $\frac{D}{R} = 4$, Figure S4a of the Supporting Information shows that the effective modulus of the skeletal structure is reduced as $\frac{w_{\mathrm{sk}}}{R}$ decreases or arc angle α increases. The strain distribution along the beam is given by

$$\varepsilon(\theta,\gamma) = \frac{N(\theta)}{\bar{E}_{\mathrm{NOA}}A^*} + \gamma\frac{M(\theta)}{\bar{E}_{\mathrm{NOA}}I^*} \tag{12}$$

where γ is the distance from the neutral axis. This strain reaches the maximum when $\theta = 0$, $\gamma = \frac{w_{\mathrm{sk}}}{2}$, and can be determined as

$$\varepsilon_{\max} = \frac{P}{EA} + \frac{w_{\mathrm{sk}}}{2}\frac{PR(1+\sin\alpha)}{EI} \tag{13}$$

or equivalently

$$\frac{\varepsilon_{\max}}{\varepsilon_{\mathrm{app}}} = 2\cos\alpha\left[\frac{(1+\sin\alpha)}{(\pi+2\alpha)(2-\cos 2\alpha)+3\sin 2\alpha}\right]\frac{w_{\mathrm{sk}}}{R} \tag{14}$$

For fixed $\xi = 0.5$, $\eta = 0.5$, and $\frac{D}{R} = 4$, Figure S4b of the Supporting Information shows that the induced maximum strain in the skeletal structure is reduced, thereby increasing the stretchability, as $\frac{w_{\mathrm{sk}}}{R}$ decreases or arc angle α increases.

Fabrication of Devices with Retroreflective Surfaces: A 15 µm thick layer of positive/negative photoresist of AZ 4620 (MicroChemicals, Germany) spin-cast at 1000 rpm, 500 rpm s^{-1} for 40 s, and soft baked at 115 °C for 180 s on a prepared silicon wafer was used for patterning. Grayscale exposure (Heidelberg MLA150) and development in AZ 400K diluted at 1:4 parts with DI water for 300 s yielded the desired structures. An inverse copy of the patterned photoresist was created by casting and thermally curing PDMS at a ratio of 10:1 of base to curing agent. The resulting PDMS structures served as molds to create an arbitrary number of replicas of the original grayscale pattern in a UV-cured optical PU (NOA 81), which were, in turn, used to produce microstructured capping layers in PU.

In Situ Measurement of Sweat in Field Trials: The experimental protocols were approved by the Institutional Review Board of Northwestern University (STU00207078). Testing involved healthy young adult volunteers during normal cycling activity with no additional human–subject risk. All subjects provided their consent prior to the test. Ethanol swabs cleaned the skin of volunteers involved in the studies, shortly before application of the microfluidic devices and absorbent pads. The subjects exercised for 20–30 min by cycling at moderate intensity. A smartphone camera (iPhone 5s; Apple, CA, USA) was used to capture pictures of the devices during testing.

Statistical Analysis: The data are reported as mean ± standard deviation (SD).

Supporting Information

Supporting Information is available from the Wiley Online Library or from the author.

Acknowledgements

J.C., S.C., and Y.D. contributed equally to this work. This work utilized Northwestern University Micro/Nano Fabrication Facility (NUFAB), which is supported in part by Soft and Hybrid Nanotechnology Experimental (SHyNE) Resource (NSF ECCS-1542205), the Materials Research Science and Engineering Center (DMR-1720139), the State of Illinois, and Northwestern University. The authors thank the Center for Bio-Integrated Electronics for support of this work. This work was supported by the National Research Foundation of Korea (NRF) grant funded by the Korea government (MSIT) (NRF-2019R1A2C1084419).

Conflict of Interest

The authors declare no conflict of interest.

Keywords

finite element analysis, material engineering, microfludic devices, sweat analysis, wearable devices

Received: April 29, 2020
Revised: June 17, 2020
Published online: September 29, 2020

[1] a) J. Heikenfeld, A. Jajack, J. Rogers, P. Gutruf, L. Tian, T. Pan, R. Li, M. Khine, J. Kim, J. Wang, J. Kim, *Lab Chip* **2018**, *18*, 217; b) J. Kim, A. S. Campbell, B. E. de Avila, J. Wang, *Nat. Biotechnol.* **2019**, *37*, 389; c) H. C. Koydemir, A. Ozcan, *Annu. Rev. Anal. Chem.* **2018**, *11*, 127; d) T. R. Ray, J. Choi, A. J. Bandodkar, S. Krishnan, P. Gutruf, L. Tian, R. Ghaffari, J. A. Rogers, *Chem. Rev.* **2019**, *119*, 5461.

[2] T. Ray, J. Choi, J. Reeder, S. P. Lee, A. J. Aranyosi, R. Ghaffari, J. A. Rogers, *Curr. Opin. Biomed. Eng.* **2019**, *9*, 47.

[3] a) A. J. Bandodkar, W. J. Jeang, R. Ghaffari, J. A. Rogers, *Annu. Rev. Anal. Chem.* **2019**, *12*, 1; b) M. Bariya, H. Y. Y. Nyein, A. Javey, *Nat. Electron.* **2018**, *1*, 160; c) J. Choi, R. Ghaffari, L. B. Baker, J. A. Rogers, *Sci. Adv.* **2018**, *4*, eaar3921; d) R. Ghaffari, J. Choi, M. S. Raj, S. Chen, S. P. Lee, J. T. Reeder, A. J. Aranyosi, A. Leech, W. H. Li, S. Schon, J. B. Model, J. A. Rogers, *Adv. Funct. Mater.* **2019**, https://doi.org/10.1002/adfm.2019072691907269; e) B. Ma, J. Chi, C. Xu, Y. Ni, C. Zhao, H. Liu, *Talanta* **2020**, *212*, 120786.

[4] G. A. Holzapfel, *Handb. Mater. Behav. Models* **2001**, *3*, 1049.

[5] a) J. Choi, A. J. Bandodkar, J. T. Reeder, T. R. Ray, A. Turnquist, S. B. Kim, N. Nyberg, A. Hourlier-Fargette, J. B. Model, A. J. Aranyosi, S. Xu, R. Ghaffari, J. A. Rogers, *ACS Sens.* **2019**, *4*, 379; b) J. Choi, D. Kang, S. Han, S. B. Kim, J. A. Rogers, *Adv. Healthcare Mater.* **2017**, *6*, 1601355; c) J. Choi, Y. Xue, W. Xia, T. R. Ray, J. T. Reeder, A. J. Bandodkar, D. Kang, S. Xu, Y. Huang, J. A. Rogers, *Lab Chip* **2017**, *17*, 2572; d) S. B. Kim, K. Lee, M. S. Raj, B. Lee, J. T. Reeder, J. Koo, A. Hourlier-Fargette, A. J. Bandodkar, S. M. Won, Y. Sekine, J. Choi, Y. Zhang, J. Yoon, B. H. Kim, Y. Yun, S. Lee, J. Shin, J. Kim, R. Ghaffari, J. A. Rogers, *Small* **2018**, *14*, 1802876; e) S. B. Kim, Y. Zhang, S. M. Won, A. J. Bandodkar, Y. Sekine, Y. Xue, J. Koo, S. W. Harshman, J. A. Martin, J. M. Park, T. R. Ray, K. E. Crawford, K. T. Lee, J. Choi, R. L. Pitsch, C. C. Grigsby, A. J. Strang, Y. Y. Chen, S. Xu, J. Kim, A. Koh, J. S. Ha, Y. Huang, S. W. Kim, J. A. Rogers, *Small* **2018**, *14*, 1703334; f) A. Koh, D. Kang, Y. Xue, S. Lee, R. M. Pielak, J. Kim, T. Hwang, S. Min, A. Banks, P. Bastien, M. C. Manco, L. Wang, K. R. Ammann, K. I. Jang, P. Won, S. Han, R. Ghaffari, U. Paik, M. J. Slepian, G. Balooch, Y. Huang, J. A. Rogers, *Sci. Transl. Med.* **2016**, *8*, 366ra165; g) Y. Sekine, S. B. Kim, Y. Zhang, A. J. Bandodkar, S. Xu, J. Choi, M. Irie, T. R. Ray, P. Kohli, N. Kozai, T. Sugita, Y. Wu, K. Lee, K. T. Lee, R. Ghaffari, J. A. Rogers, *Lab Chip* **2018**, *18*, 2178.

[6] D. H. Kim, N. S. Lu, R. Ma, Y. S. Kim, R. H. Kim, S. D. Wang, J. Wu, S. M. Won, H. Tao, A. Islam, K. J. Yu, T. I. Kim, R. Chowdhury, M. Ying, L. Z. Xu, M. Li, H. J. Chung, H. Keum, M. McCormick, P. Liu, Y. W. Zhang, F. G. Omenetto, Y. G. Huang, T. Coleman, J. A. Rogers, *Science* **2011**, *333*, 838.

[7] Y. H. Zhang, H. R. Fu, Y. W. Su, S. Xu, H. Y. Cheng, J. A. Fan, K. C. Hwang, J. A. Rogers, Y. G. Huang, *Acta Mater.* **2013**, *61*, 7816.

[8] P. E. Keller, R. Kouzes, *Water Vapor Permeation in Plastics*, Pacific Northwest National Laboratory, Richland, WA **2017**.